Segmented Crystal Analyzer with Image Acquisition in 2D (SCANIA-2D)

X-RAY EMISSION SPECTROMETER AT BALDER BEAMLINE

I. CONCEPTUAL DESIGN REPORT

Konstantin Klementiev

The MAX IV Laboratory

17 Nov 2014

About the front page logo:

The central part is taken from the coat of arms of *Scania*, the southernmost province (landskap) of Sweden, with modified colors of the crown and the griffin's tongue. The logo symbolizes 2D positional image analysis with an added color axis (energy). 2D image analysis is in the core of the presented spectrometer and is essential for a good spectral resolution.

Contents

1 Overview

This document describes the x-ray emission spectrometer to be installed at the Balder beamline. It features (i) large energy range 2–30 keV; (ii) energy resolution much better than the natural widths of Kα and Kβ lines for elements S trough Ru; (iii) ample space for the insertion of large sample setups due to the positioning of the detector *under* the sample; (iv) energy dispersive images exempt from necessity of doing θ-2θ scans; the energy dispersion is possible in a large scale and is controlled by the in-Rowland-circle positioning of the fluorescence source; (v) backward scattering (emission) from the sample, which (a) makes the usual side window in in-situ cells or sample vacuum volume not necessary, (b) has no depth related increase of the fluorescence source and (c) facilitates the polarization dependent studies (enables exact sample positioning relative to the polarization plane).

The spectrometer is based on the Rowland circle geometry with three exchangeable sets of crystals: Si(111), Si(220) and Si(400). Each set has 4 crystals which are of Johansson type in the meridional direction and flat in the sagittal direction. The total acceptance angle is from 0.2v×0.2h rad² to 0.2v×0.3h rad² depending on the Bragg angle.

The present CDR is a base for the upcoming Technical Design Report.

2 Introduction

Modern x-ray emission spectrometers are mostly based on the so called Rowland circle geometry that allows for simultaneous focusing and energy discrimination. In this geometry the source (sample), the analyzing crystal and the detector lie on the Rowland circle and the crystal is bent, usually spherically, with the bending radius equal to the doubled radius of the Rowland circle. For better energy resolution and focusing the Bragg angle is usually attempted to be close to 90°. This has the following drawbacks:

- The sample-to-detector distance is small at θ≈90° (d_{SD}=2Rsin2θ, R is the Rowland circle radius). This makes impossible to use many required sample infrastructures: in-situ cells, cryostats, magnets, etc.
- Only a few fortunate combinations "a fluorescence line of an element" + "available crystals" result in θ≈90°. For example, the maximum θ over all available silicon cuts (111) through (10,10,0) for Kα1 lines of elements S through Nb is 89.35° (Ge Kα1 with Si(555) or Si(751), see Table 1), but it is only 71.59° in average for these elements.

Therefore, it is very desirable that the spectrometer could work at *Bragg angles* far from 90°.

A usual *positioning* of the analyzing crystal is at 90° to the beam with the sample surface being at 45° to both the incident and emitted beams. An obvious drawback of this geometry is that it requires an *ad hoc* side window in the sample vacuum volume, in-situ cells and cryostats.

An original spectrometer design was proposed at Alba/CLÆSS beamline, named as CLEAR spectrometer [1] that can work at relatively small Bragg angles and in back scattering. The back scattering geometry may potentially have a drawback related to Compton scattering, which will be discussed in Appendix A, but it definitely has a big advantage: it can work with any transmission setup (e.g. chemical cells, diamond anvil cells, cryostats) typical at a usual EXAFS beamline. CLEAR has variable sagittal crystal bending that depends on Bragg angle. This feature has two great advantages:

- Each part of the crystal lies on its Rowland circle, i.e. the whole crystal spans a fan of Rowland circles all having two common points: the source (sample) and the detector center. Thus the whole crystal surface works for a given energy – in the meridional direction this is true because the crystal is Johansson-like – and the crystal has both the best possible energy resolution and the best possible efficiency.
- The energy dispersive image at the detector is one-dimensional, thus allowing the usage of a 1D, and not an otherwise required 2D, position sensitive detector, which is especially important for the in-vacuum design owing to the compactness and low power consumption of a 1D detector.

On the other hand, the variable sagittal bending also had a strong impact onto the design, assembling and commissioning of CLEAR. The three-fold curvature of the crystal required a complex cutting and assembling procedure, special high precision assembling tools and motorized benders. The complexity of the energy change in CLEAR also implies long commissioning with x-rays and thus losses in beam time for other applications.

The aim of the present design is to reduce the complexity of CLEAR while keeping the overall back scattering geometry. The main simplification is in the treatment of the sagittal divergence of the emission beam. The too complex sagittal crystal bending is proposed to be replaced by two alternative solutions: sagittal collimation with a whispering gallery collimator (Section 4) and sagittal segmentation of the crystal (Section 5). The crystals here are always sagittally flat.

The design studies were done with the software xrt [2] that is capable of doing ray tracing (i) at multiple reflections on same surface and (ii) with several non-sequential surfaces.

3 Geometry of the spectrometer

In the present design, only the most usual crystals are considered: silicon and germanium.

The upper limit for Bragg angle is defined such that the sample-detector distance be reasonably large for a detector positioned under the sample, here >300 mm. For a Rowland circle diameter of 1.5 m (see below) this results in θ_{max}=84°.

The cuts (111) and (220) together with their harmonics (green and magenta colors in Table 1) cover the energies 2–~22 keV if θ_{min}=48°. The exceptions are at very low energies (Cl and Ar) and for first few 3d elements: Ti, V, Cr and Mn. As the last ones are very common for a beamline like Balder, a third crystal has to be considered. As seen in Table 1, the (400) cut is the best suitable (blue color).

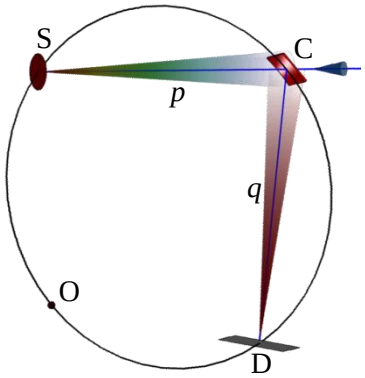

Figure 1. The scattering geometry. S = source (sample), C = crystal analyzer, D = detector, O = curvature center for C.

Sample-detector distance: $d_{SD} = D_R \sin 2\theta$,
where D_R is Rowland circle diameter, here 1.5 m,

$p = q = D_R \sin\theta$

A 3D conceptual view is depicted in Figure 1. The diffraction plane (Rowland circle) is vertical because the beam size at the sample is smaller vertically than horizontally. One of the most important improvements in the proposed design is *the bottom position of the detector*, as it gives much more space around the sample and thus more freedom in selecting the sample environment.

As shown in Figure 2, the lowest detector position is at ~55°. As this angle is in the range of interest, it defines the diameter of the Rowland circle. The height of the sample at Balder is about 1340 mm above the floor and hence the maximum diameter is ~1.5 m, which gives the detector center at ~180 mm above the floor. The crystal-to-detector distance can be reduced by utilizing asymmetrically cut crystals as $q = D_R \sin(\theta-\alpha)$, and thus a larger D_R (the Rowland circle diameter) is possible. However, this approach would require several crystals with various asymmetry angles α for working at various ranges of θ angles. For practical reasons, the crystals in the present design are considered to be symmetrically cut.

Table 1. Bragg angles for $K\alpha_1$, $K\beta_1$ and K-edges for Si and Ge crystals.

			Si (111)	Si (220)	Si (311)	Si (400)	Si (331)	Si (422)	Si (333, 511)	Si (440)	Si (444)	Si (660)	Si (555, 751)	Si (880)	Si (777)	Si (888)	Si (10, 10,0)	Ge (111)	Ge (220)	Ge (311)	Ge (400)	Ge (331)	Ge (422)	Ge (333, 511)	Ge (440)	Ge (444)	Ge (660)	Ge (555, 751)	Ge (880)	Ge (777)	Ge (888)	Ge (10, 10,0)
		d (Å)	3.1354	1.9200	1.6374	1.3577	1.2459	1.1085	1.0451	0.9600	0.7839	0.6400	0.6271	0.4800	0.4479	0.3919	0.3840	3.2663	2.0002	1.7058	1.4143	1.2979	1.1548	1.0888	1.0001	0.8166	0.6667	0.6533	0.5000	0.4666	0.4083	0.4000
No.	Elem.	**Kα1**																													
16	S	2307.84	58.95															55.32													
17	Cl	2622.39	48.93															46.36													
18	Ar	2957.7	41.95															39.92													
19	K	3313.8	36.63	76.99														34.94	69.27												
20	Ca	3691.68	32.38	61.00														30.94	57.09	79.88											
21	Sc	4090.6	28.90	52.12	67.75													27.64	49.26	62.68											
22	Ti	4510.84	26.00	45.71	57.07													24.88	43.40	53.68	76.33										
23	V	4952.2	23.53	40.69	49.86	67.22												22.54	38.74	47.21	62.26	74.69									
24	Cr	5414.72	21.42	36.60	44.36	57.49	66.77											20.52	34.92	42.16	54.05	61.90	82.48								
25	Mn	5898.75	19.58	33.19	39.93	50.72	57.51	71.45										18.77	31.70	38.03	47.99	54.07	65.51	74.85							
26	Fe	6403.84	17.98	30.28	36.24	45.48	50.99	60.84	67.86									17.24	28.95	34.58	43.19	48.23	56.96	62.76	75.46						
27	Co	6930.32	16.58	27.77	33.11	41.21	45.89	53.80	58.86	68.71								15.89	26.57	31.63	39.23	43.57	50.77	55.24	63.43						
28	Ni	7478.15	15.33	25.58	30.42	37.63	41.71	48.40	52.48	59.71								14.70	24.48	29.08	35.88	39.70	45.88	49.59	55.99						
29	Cu	8047.78	14.22	23.65	28.06	34.57	38.19	44.02	47.48	53.36	79.33							13.64	22.65	26.85	33.00	36.41	41.84	45.03	50.37	70.62					
30	Zn	8638.86	13.23	21.95	25.99	31.91	35.17	40.34	43.36	48.37	66.27							12.69	21.02	24.88	30.49	33.57	38.42	41.23	45.85	61.50					
31	Ga	9251.74	12.34	20.43	24.16	29.57	32.54	37.19	39.88	44.26	58.74							11.84	19.57	23.13	28.28	31.08	35.47	37.98	42.07	55.14					
32	Ge	9886.42	11.54	19.06	22.52	27.51	30.22	34.45	36.87	40.78	53.13	78.45	89.35					11.07	18.27	21.57	26.32	28.89	32.89	35.16	38.83	50.17	70.13	73.71			
33	As	10543.7	10.81	17.83	21.04	25.66	28.16	32.03	34.23	37.77	48.60	66.73	69.65					10.37	17.09	20.16	24.56	26.94	30.61	32.69	36.01	46.06	61.87	64.16			
34	Se	11222.4	10.15	16.72	19.72	24.01	26.32	29.89	31.91	35.13	44.81	59.67	61.75					9.74	16.03	18.90	22.99	25.19	28.58	30.49	33.53	42.57	55.95	57.74			
35	Br	11924.2	9.54	15.71	18.51	22.51	24.66	27.97	29.83	32.79	41.55	54.32	56.00					9.16	15.07	17.75	21.57	23.61	26.76	28.52	31.32	39.54	51.24	52.73			
36	Kr	12649	8.99	14.79	17.42	21.16	23.16	26.24	27.96	30.70	38.70	49.97	51.40					8.63	14.18	16.70	20.27	22.19	25.11	26.75	29.34	36.88	47.31	48.61	78.55		
37	Rb	13395.3	8.49	13.95	16.42	19.93	21.81	24.68	26.28	28.82	36.19	46.31	47.56	74.61				8.15	13.38	15.74	19.10	20.89	23.63	25.15	27.56	34.52	43.96	45.11	67.74	82.66	
38	Sr	14165	8.02	13.18	15.50	18.80	20.56	23.25	24.76	27.12	33.94	43.14	44.26	65.75	77.70			7.70	12.64	14.87	18.03	19.71	22.27	23.70	25.95	32.41	41.03	42.06	61.07	69.70	
39	Y	14958.4	7.60	12.47	14.66	17.77	19.43	21.95	23.36	25.57	31.92	40.36	41.37	59.70	67.70			7.29	11.96	14.06	17.04	18.62	21.03	22.37	24.48	30.50	38.43	39.38	55.97	62.64	
40	Zr	15775.1	7.20	11.81	13.89	16.82	18.39	20.76	22.09	24.16	30.09	37.88	38.80	54.95	61.32			6.91	11.33	13.32	16.13	17.62	19.89	21.16	23.14	28.77	36.12	36.98	51.80	57.37	74.26	79.22
41	Nb	16615.1	6.83	11.21	13.17	15.95	17.43	19.67	20.92	22.87	28.42	35.66	36.51	51.01	56.41	72.17	76.32	6.56	10.75	12.63	15.30	16.71	18.85	20.04	21.91	27.19	34.03	34.83	48.26	53.09	66.04	68.86
42	Mo	17479.3	6.49	10.64	12.51	15.14	16.54	18.66	19.84	21.68	26.90	33.65	34.44	47.63	52.35	64.81	67.45	6.23	10.21	12.00	14.52	15.86	17.89	19.01	20.77	25.74	32.14	32.88	45.17	49.47	60.30	62.45
43	Tc	18367.1	6.18	10.12	11.90	14.39	15.72	17.73	18.84	20.58	25.50	31.83	32.56	44.68	48.90	59.45	61.51	5.93	9.71	11.41	13.81	15.07	16.99	18.06	19.72	24.41	30.41	31.11	42.45	46.33	55.76	57.53
44	Ru	19279.2	5.89	9.64	11.33	13.70	14.96	16.86	17.92	19.57	24.22	30.16	30.85	42.06	45.88	55.13	56.86	5.65	9.25	10.87	13.14	14.34	16.17	17.18	18.75	23.19	28.83	29.49	40.02	43.56	51.96	53.49
45	Rh	20216.1	5.61	9.19	10.79	13.05	14.25	16.06	17.06	18.63	23.03	28.63	29.28	39.70	43.20	51.48	52.99	5.39	8.82	10.36	12.52	13.67	15.40	16.36	17.86	22.06	27.38	28.00	37.82	41.09	48.68	50.05
46	Pd	21177.1	5.36	8.77	10.30	12.45	13.59	15.31	16.27	17.75	21.93	27.22	27.83	37.58	40.81	48.32	49.67	5.14	8.42	9.88	11.95	13.03	14.68	15.60	17.02	21.01	26.04	26.62	35.83	38.86	45.81	47.03
47	Ag	22162.9	5.12	8.38	9.84	11.89	12.97	14.62	15.52	16.94	20.91	25.92	26.49	35.64	38.64	45.54	46.75	4.91	8.04	9.44	11.41	12.45	14.02	14.89	16.24	20.03	24.80	25.35	34.01	36.83	43.24	44.36
48	Cd	23173.6	4.89	8.01	9.40	11.36	12.40	13.96	14.83	16.18	19.95	24.71	25.25	33.87	36.67	43.04	44.16	4.70	7.69	9.02	10.90	11.89	13.39	14.22	15.51	19.12	23.66	24.17	32.34	34.98	40.94	41.97
49	In	24209.7	4.68	7.66	9.00	10.87	11.86	13.36	14.18	15.47	19.07	23.58	24.10	32.24	34.87	40.79	41.82	4.50	7.36	8.63	10.43	11.38	12.81	13.60	14.84	18.28	22.59	23.08	30.80	33.28	38.84	39.80

			Si (111)	Si (220)	Si (311)	Si (400)	Si (331)	Si (422)	Si (333, 511)	Si (440)	Si (444)	Si (660)	Si (555, 751)	Si (880)	Si (777)	Si (888)	Si (10, 10,0)	Ge (111)	Ge (220)	Ge (311)	Ge (400)	Ge (331)	Ge (422)	Ge (333, 511)	Ge (440)	Ge (444)	Ge (660)	Ge (555, 751)	Ge (880)	Ge (777)	Ge (888)	Ge (10, 10,0)
		d (Å)	3.1354	1.9200	1.6374	1.3577	1.2459	1.1085	1.0451	0.9600	0.7839	0.6400	0.6271	0.4800	0.4479	0.3919	0.3840	3.2663	2.0002	1.7058	1.4143	1.2979	1.1548	1.0888	1.0001	0.8166	0.6667	0.6533	0.5000	0.4666	0.4083	0.4000
No.	Elem.	**Kβ1**																													
16	S	2464.04	53.36															50.38													
17	Cl	2815.6	44.60															42.38													
18	Ar	3190.5	38.29															36.50	76.27												
19	K	3589.6	33.42	64.09														31.92	59.70												
20	Ca	4012.7	29.52	53.57	70.65													28.23	50.57	64.92											
21	Sc	4460.5	26.31	46.37	58.08													25.18	44.01	54.56	79.31										
22	Ti	4931.81	23.63	40.89	50.14	67.79												22.63	38.93	47.47	62.72	75.58									
23	V	5427.29	21.36	36.51	44.23	57.28	66.46											20.47	34.82	42.04	53.86	61.65	81.54								
24	Cr	5946.71	19.42	32.88	39.54	50.16	56.80	70.12	85.90									18.61	31.41	37.67	47.48	53.44	64.52	73.23							
25	Mn	6490.45	17.74	29.83	35.68	44.71	50.05	59.50	66.05	84.21								17.00	28.52	34.05	42.48	47.38	55.80	61.31	72.75						
26	Fe	7057.98	16.27	27.22	32.44	40.31	44.83	52.40	57.18	66.19								15.60	26.05	30.99	38.39	42.59	49.52	53.78	61.43						
27	Co	7649.43	14.98	24.97	29.67	36.65	40.58	46.98	50.84	57.58								14.37	23.90	28.37	34.96	38.64	44.57	48.10	54.13	82.96					
28	Ni	8264.66	13.84	23.00	27.26	33.54	37.02	42.58	45.86	51.38	73.12							13.28	22.02	26.09	32.03	35.31	40.51	43.55	48.59	66.72					
29	Cu	8905.29	12.83	21.26	25.16	30.85	33.97	38.90	41.76	46.48	62.63							12.31	20.37	24.09	29.48	32.44	37.07	39.75	44.11	58.48					
30	Zn	9572	11.92	19.71	23.30	28.49	31.32	35.75	38.29	42.42	55.71							11.44	18.89	22.31	27.25	29.93	34.11	36.50	40.36	52.48	76.26	82.48			
31	Ga	10264.2	11.11	18.33	21.64	26.41	29.00	33.01	35.30	38.98	50.40	70.68	74.39					10.66	17.58	20.74	25.28	27.73	31.53	33.69	37.15	47.70	64.94	67.60			
32	Ge	10982.1	10.37	17.10	20.17	24.57	26.94	30.61	32.69	36.01	46.07	61.88	64.18					9.95	16.39	19.33	23.52	25.78	29.26	31.23	34.36	43.73	57.85	59.78			
33	As	11726.2	9.71	15.98	18.84	22.92	25.11	28.48	30.39	33.41	42.41	55.69	57.46					9.31	15.33	18.05	21.95	24.04	27.24	29.05	31.91	40.35	52.46	54.03			
34	Se	12495.9	9.10	14.97	17.64	21.43	23.47	26.59	28.34	31.12	39.26	50.82	52.29					8.74	14.36	16.91	20.53	22.47	25.44	27.11	29.74	37.41	48.08	49.41	82.80		
35	Br	13291.4	8.55	14.06	16.55	20.09	21.98	24.88	26.50	29.07	36.51	46.78	48.05	76.33				8.21	13.48	15.87	19.25	21.06	23.82	25.37	27.80	34.83	44.39	45.56	68.86	88.31	
36	Kr	14112	8.05	13.23	15.56	18.88	20.65	23.35	24.85	27.23	34.08	43.34	44.47	66.23	78.73			7.73	12.69	14.92	18.10	19.78	22.36	23.80	26.06	32.55	41.21	42.26	61.46	70.30	
37	Rb	14961.3	7.59	12.46	14.66	17.77	19.43	21.95	23.36	25.57	31.91	40.35	41.36	59.68	67.68			7.29	11.96	14.06	17.04	18.62	21.03	22.37	24.48	30.49	38.42	39.37	55.96	62.62	
38	Sr	15835.7	7.17	11.76	13.83	16.76	18.31	20.68	22.00	24.07	29.96	37.71	38.63	54.64	60.92	87.23		6.88	11.29	13.27	16.07	17.56	19.82	21.07	23.04	28.65	35.96	36.82	51.52	57.03	73.50	78.12
39	Y	16737.8	6.78	11.12	13.07	15.83	17.29	19.52	20.76	22.69	28.20	35.36	36.20	50.50	55.78	70.91	74.69	6.51	10.67	12.54	15.18	16.58	18.71	19.89	21.74	26.97	33.75	34.54	47.79	52.54	65.11	67.80
40	Zr	17667.8	6.43	10.53	12.37	14.98	16.36	18.45	19.62	21.44	26.59	33.25	34.02	46.97	51.57	63.54	66.02	6.17	10.10	11.87	14.36	15.68	17.69	18.80	20.54	25.45	31.75	32.49	44.56	48.76	59.25	61.30
41	Nb	18622.5	6.09	9.98	11.73	14.19	15.50	17.48	18.57	20.29	25.13	31.34	32.06	43.91	48.00	58.14	60.10	5.85	9.58	11.25	13.61	14.86	16.75	17.80	19.44	24.06	29.95	30.64	41.74	45.51	54.62	56.32
42	Mo	19608.3	5.79	9.48	11.13	13.47	14.70	16.57	17.61	19.23	23.79	29.60	30.28	41.20	44.90	53.77	55.42	5.55	9.09	10.68	12.92	14.10	15.89	16.88	18.43	22.78	28.31	28.94	39.22	42.65	50.75	52.21
43	Tc	20619	5.50	9.01	10.58	12.79	13.96	15.74	16.72	18.25	22.55	28.02	28.65	38.78	42.16	50.10	51.53	5.28	8.65	10.15	12.27	13.39	15.09	16.03	17.50	21.60	26.80	27.40	36.96	40.12	47.42	48.73
44	Ru	21656.8	5.24	8.57	10.07	12.17	13.28	14.96	15.90	17.35	21.42	26.57	27.16	36.61	39.72	46.92	48.20	5.03	8.23	9.66	11.68	12.74	14.35	15.24	16.63	20.52	25.43	25.99	34.92	37.84	44.52	45.69
45	Rh	22723.6	4.99	8.17	9.59	11.59	12.65	14.25	15.13	16.51	20.37	25.23	25.79	34.63	37.52	44.11	45.27	4.79	7.84	9.20	11.12	12.13	13.66	14.51	15.83	19.52	24.15	24.68	33.06	35.78	41.93	43.00
46	Pd	23818.7	4.76	7.79	9.15	11.05	12.06	13.58	14.42	15.73	19.39	24.00	24.52	32.83	35.53	41.61	42.67	4.57	7.48	8.78	10.60	11.57	13.03	13.83	15.08	18.59	22.98	23.48	31.36	33.90	39.60	40.59
47	Ag	24942.4	4.55	7.44	8.73	10.55	11.51	12.96	13.76	15.00	18.49	22.85	23.35	31.18	33.70	39.36	40.33	4.36	7.14	8.38	10.12	11.04	12.43	13.20	14.39	17.72	21.89	22.36	29.80	32.18	37.50	38.41
48	Cd	26095.5	4.35	7.11	8.34	10.08	10.99	12.37	13.14	14.33	17.64	21.79	22.26	29.66	32.03	37.31	38.22	4.17	6.82	8.01	9.67	10.55	11.87	12.60	13.74	16.91	20.87	21.32	28.36	30.60	35.58	36.43
49	In	27275.9	4.16	6.80	7.98	9.64	10.51	11.83	12.56	13.69	16.85	20.80	21.25	28.26	30.49	35.44	36.29	3.99	6.52	7.66	9.25	10.09	11.35	12.05	13.14	16.16	19.93	20.36	27.03	29.15	33.83	34.62

			Si (111)	Si (220)	Si (311)	Si (400)	Si (331)	Si (422)	Si (333, 511)	Si (440)	Si (444)	Si (660)	Si (555, 751)	Si (880)	Si (777)	Si (888)	Si (10, 10,0)	Ge (111)	Ge (220)	Ge (311)	Ge (400)	Ge (331)	Ge (422)	Ge (333, 511)	Ge (440)	Ge (444)	Ge (660)	Ge (555, 751)	Ge (880)	Ge (777)	Ge (888)	Ge (10, 10,0)
		d (Å)	3.1354	1.9200	1.6374	1.3577	1.2459	1.1085	1.0451	0.9600	0.7839	0.6400	0.6271	0.4800	0.4479	0.3919	0.3840	3.2663	2.0002	1.7058	1.4143	1.2979	1.1548	1.0888	1.0001	0.8166	0.6667	0.6533	0.5000	0.4666	0.4083	0.4000
No.	Elem.	**K-edge**																													
16	S	2472	53.11															50.15													
17	Cl	2822.4	44.47															42.26													
18	Ar	3205.9	38.08															36.30	75.19												
19	K	3608.4	33.23	63.48														31.73	59.20												
20	Ca	4038.5	29.31	53.08	69.63													28.03	50.13	64.15											
21	Sc	4492	26.11	45.95	57.44													24.99	43.63	54.00	77.36										
22	Ti	4966	23.46	40.55	49.67	66.85												22.47	38.62	47.04	61.96	74.12									
23	V	5465	21.21	36.21	43.85	56.67	65.57											20.32	34.55	41.68	53.32	60.93	79.20								
24	Cr	5989	19.28	32.62	39.21	49.68	56.18	69.03	82.05									18.48	31.16	37.36	47.04	52.89	63.68	71.94							
25	Mn	6539	17.60	29.59	35.38	44.29	49.55	58.78	65.11	80.94								16.87	28.29	33.76	42.09	46.92	55.18	60.55	71.43						
26	Fe	7112	16.14	27.00	32.16	39.94	44.40	51.84	56.51	65.22								15.48	25.84	30.73	38.05	42.19	49.01	53.19	60.64						
27	Co	7709	14.86	24.76	29.41	36.32	40.20	46.50	50.30	56.89								14.25	23.71	28.13	34.65	38.29	44.14	47.61	53.52	80.00					
28	Ni	8333	13.73	22.80	27.02	33.23	36.66	42.15	45.38	50.80	71.64							13.17	21.83	25.86	31.74	34.97	40.11	43.10	48.06	65.65					
29	Cu	8979	12.72	21.07	24.94	30.57	33.65	38.52	41.35	45.99	61.74							12.20	20.19	23.88	29.22	32.14	36.72	39.36	43.66	57.73					
30	Zn	9659	11.81	19.53	23.08	28.21	31.01	35.38	37.89	41.95	54.96							11.33	18.72	22.10	26.99	29.64	33.76	36.12	39.92	51.81	74.29	79.26			
31	Ga	10367	10.99	18.15	21.42	26.13	28.68	32.64	34.90	38.53	49.72	69.12	72.47					10.55	17.40	20.52	25.01	27.43	31.19	33.31	36.72	47.08	63.75	66.26			
32	Ge	11103	10.26	16.91	19.94	24.28	26.62	30.24	32.29	35.56	45.42	60.74	62.92					9.84	16.21	19.11	23.25	25.48	28.91	30.85	33.94	43.14	56.87	58.73			
33	As	11867	9.59	15.79	18.60	22.63	24.79	28.12	29.99	32.97	41.79	54.71	56.41					9.20	15.14	17.83	21.68	23.73	26.90	28.67	31.49	39.77	51.58	53.10			
34	Se	12658	8.99	14.78	17.40	21.14	23.15	26.22	27.94	30.67	38.67	49.93	51.35					8.62	14.17	16.69	20.26	22.17	25.09	26.73	29.32	36.85	47.27	48.56	78.35		
35	Br	13474	8.44	13.86	16.32	19.81	21.67	24.52	26.12	28.64	35.94	45.96	47.20	73.43				8.10	13.30	15.65	18.98	20.76	23.48	25.00	27.39	34.29	43.64	44.77	66.94	80.41	
36	Kr	14326	7.93	13.02	15.32	18.59	20.32	22.98	24.46	26.79	33.51	42.54	43.63	64.35	75.03			7.61	12.49	14.70	17.82	19.48	22.01	23.42	25.64	32.00	40.47	41.48	59.93	68.03	
37	Rb	15200	7.47	12.26	14.42	17.48	19.11	21.59	22.97	25.14	31.35	39.59	40.57	58.17	65.58			7.17	11.77	13.83	16.76	18.31	20.68	22.00	24.07	29.96	37.71	38.63	54.65	60.93	87.34	
38	Sr	16105	7.05	11.56	13.60	16.47	18.00	20.32	21.61	23.64	29.41	36.97	37.87	53.31	59.25	79.15		6.77	11.10	13.04	15.79	17.25	19.47	20.70	22.64	28.12	35.26	36.10	50.33	55.58	70.52	74.20
39	Y	17038	6.66	10.92	12.84	15.54	16.98	19.16	20.37	22.27	27.66	34.65	35.47	49.29	54.32	68.18	71.35	6.40	10.48	12.32	14.91	16.28	18.37	19.52	21.33	26.46	33.07	33.85	46.69	51.24	63.02	65.44
40	Zr	17998	6.31	10.33	12.14	14.70	16.05	18.10	19.24	21.03	26.07	32.56	33.32	45.85	50.26	61.50	63.76	6.05	9.92	11.65	14.10	15.39	17.35	18.44	20.15	24.95	31.11	31.82	43.54	47.58	57.52	59.43
41	Nb	18986	5.98	9.79	11.50	13.92	15.19	17.13	18.20	19.88	24.62	30.68	31.38	42.86	46.80	56.42	58.24	5.74	9.40	11.04	13.35	14.57	16.42	17.45	19.06	23.57	29.32	29.99	40.77	44.41	53.10	54.71
42	Mo	20000	5.67	9.29	10.91	13.20	14.41	16.24	17.25	18.84	23.29	28.97	29.62	40.22	43.79	52.27	53.82	5.45	8.91	10.47	12.66	13.82	15.57	16.54	18.06	22.31	27.70	28.33	38.31	41.63	49.39	50.79
43	Tc	21044	5.39	8.83	10.36	12.53	13.68	15.41	16.37	17.87	22.07	27.40	28.02	37.86	41.12	48.73	50.10	5.17	8.47	9.94	12.02	13.12	14.78	15.70	17.13	21.15	26.22	26.80	36.09	39.15	46.18	47.43
44	Ru	22117	5.13	8.39	9.86	11.91	13.00	14.65	15.56	16.98	20.95	25.97	26.55	35.73	38.74	45.66	46.88	4.92	8.06	9.46	11.43	12.47	14.05	14.92	16.28	20.08	24.86	25.41	34.09	36.92	43.35	44.48
45	Rh	23220	4.88	7.99	9.38	11.34	12.37	13.94	14.80	16.15	19.91	24.65	25.20	33.79	36.59	42.94	44.05	4.69	7.67	9.00	10.88	11.87	13.37	14.19	15.48	19.08	23.61	24.12	32.27	34.90	40.84	41.87
46	Pd	24350	4.66	7.62	8.94	10.81	11.79	13.28	14.10	15.38	18.95	23.44	23.95	32.03	34.64	40.51	41.53	4.47	7.31	8.58	10.37	11.31	12.74	13.52	14.75	18.17	22.45	22.94	30.61	33.07	38.58	39.52
47	Ag	25514	4.44	7.27	8.53	10.31	11.25	12.66	13.44	14.66	18.06	22.31	22.80	30.41	32.85	38.31	39.25	4.27	6.98	8.19

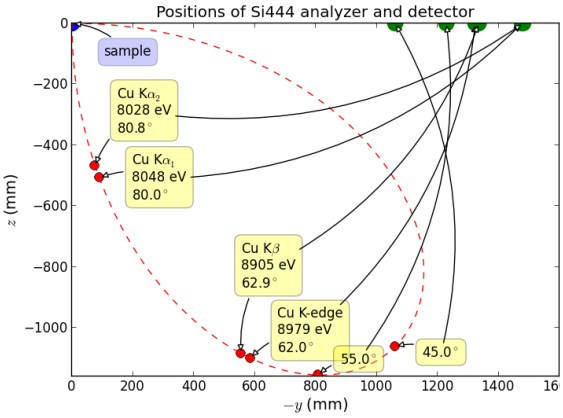

Figure 2. Positions for the Si444 crystal and the detector at the excitation at the Cu K-edge. The detector coordinates are given by:

$y = -d_{SD} \cos\theta$,
$z = -d_{SD} \sin\theta$,
where $d_{SD} = D_R \sin 2\theta$.

4 Working with sagittal divergence A: whispering gallery collimator

Whispering gallery is a curved surface that reflects waves (historically – sounds) along itself with very low attenuation [3]. The physical reason for this effect is good reflectivity at small grazing incidence angles. The effect also works for x-rays where the reflectivity coefficient is close to 1 at the incidence angles below a few mrad. The desired angular acceptance of a fluorescence beam is at least 10°. Therefore, a whispering gallery collimator should consist of several tens of bent plates, where each of them accepts an angle of a few mrad.

Define the sagittal plane to be orthogonal to the Rowland circle and containing the fluorescence source (sample) and the detector center. In the present case this plane is horizontal. In the sagittal plane such a whispering gallery collimator can look as in Figure 3, where the geometrical parameters are so far non-optimal. In the meridional plane (Rowland circle plane) the beam is simply divergent. In the following sections the general properties of the collimator will be considered and then the collimator will be optimized in focal length, length of the plates, material, required roughness and the maximum angular acceptance.

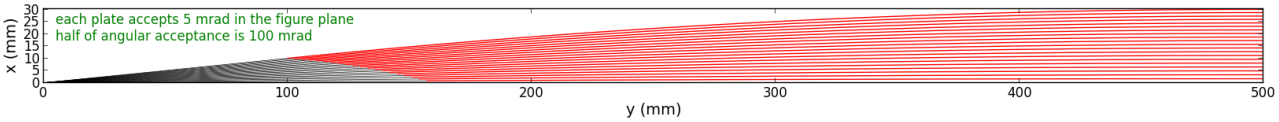

Figure 3. Whispering gallery collimator: cross-section in the sagittal plane. Here the plates (red lines) are spaced such that each one accepts 5 mrad of the fluorescence beam emitted from the xy origin. The spacing at the right end is from 1.3 to 1.6 mm and at the left end is ~0.5 mm. The plates are bent as parabolic cylinders such that the left end tangents are directed towards the source and the right end ones are parallel to the y axis.

4.1 Performance of a single collimating plate

A mirror coated by a heavy material can accept a beam with a wider divergence because it has a larger critical angle at a given energy, see Figure 4. However, the reflectivity coefficient at small angles is higher for a lighter material. This difference becomes even more pronounced at multiple reflections as the reflectivity coefficient is raised to power N – the number of reflections. Therefore, it is difficult to assess the material efficiency *a priory*, without ray tracing.

During the propagation over a plate the beam is reflected multiple times. The number of reflections, the incidence angles and the elevation of the beam over the plate depend on the reflecting material and the focal distance f, as can be observed in Figures 5–7. Here, a single collimating plate accepts 5 mrad of incoming beam and deflects it by 100 mrad. The plate length was fixed to $0.8f$. Zero of the local y axis was then at $0.2f$ from the source. The beam had energy 9 keV.

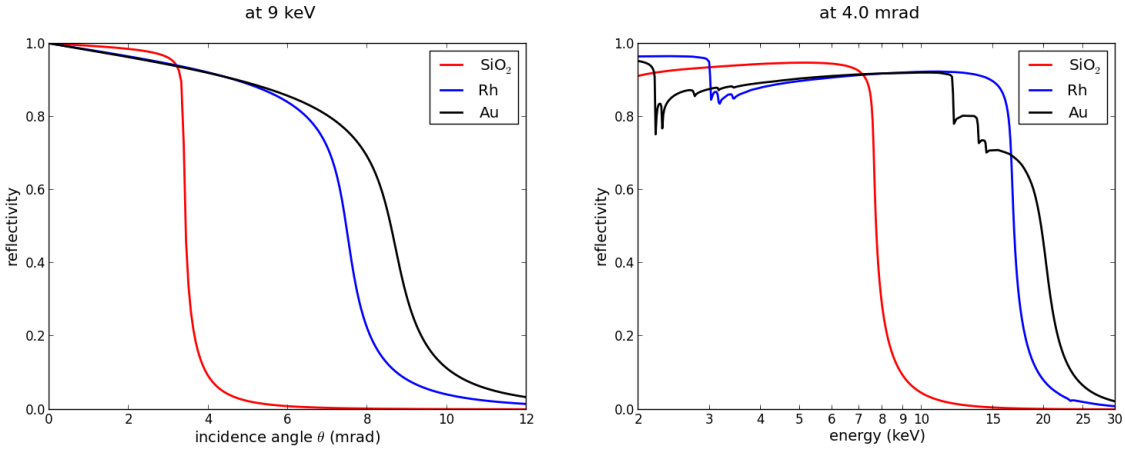

Figure 4. Reflectivity coefficient of 3 selected materials vs. incidence angle (left) and vs. energy (right).

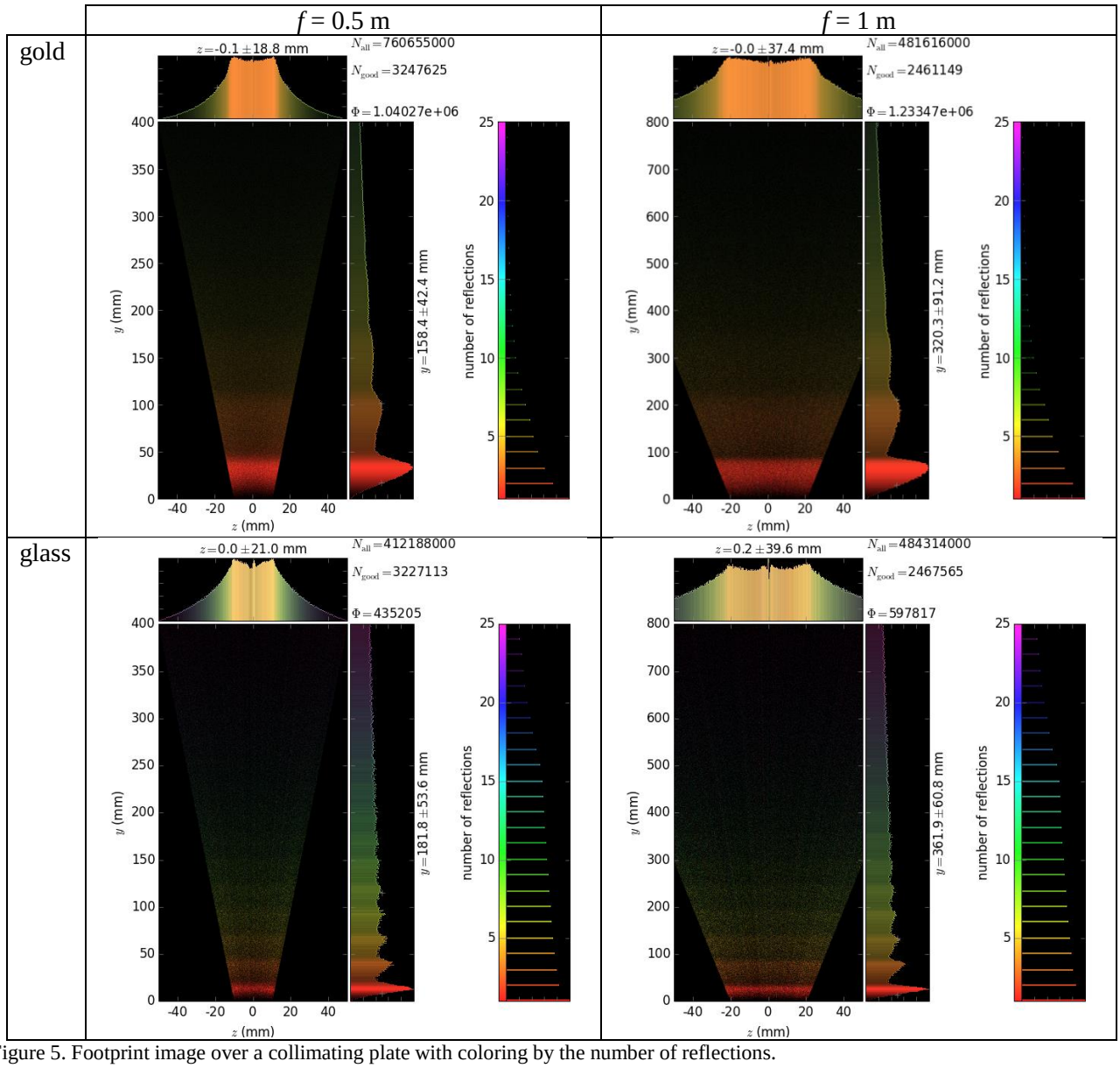

Figure 5. Footprint image over a collimating plate with coloring by the number of reflections.

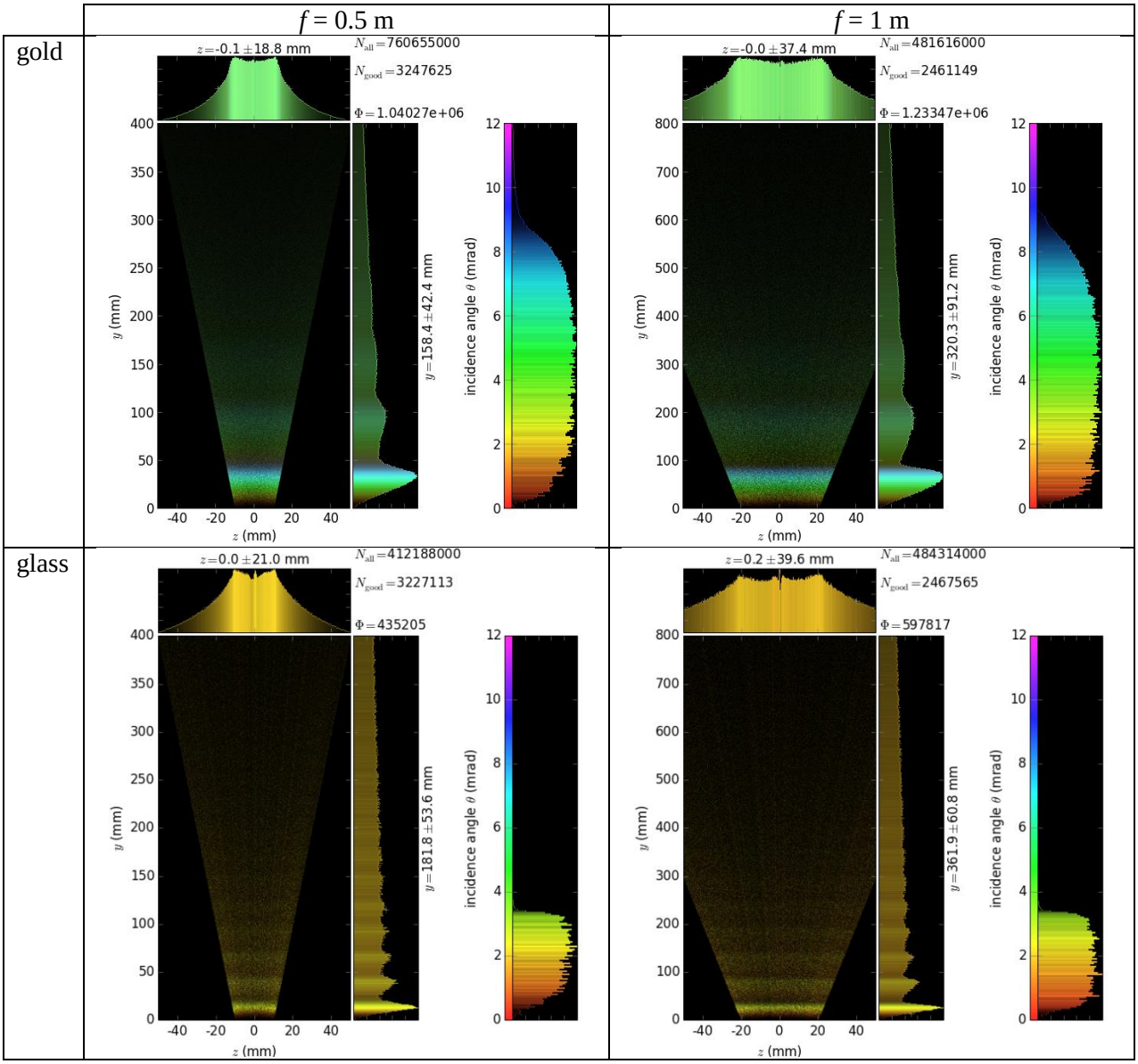

Figure 6. Footprint image over a collimating plate with coloring by incidence angle.

The local beam distributions in Figures 5–7 can be summarized as follows:

1) Compared to a golden plate, a glass plate has (a) more reflections on it, (b) smaller incidence angles and (c) lower beam elevation over the surface.

2) The overall efficiency of a heavy-material plate is higher. However, due to the own absorption edges of a heavy coating (and correspondingly the fluorescence lines) one would need two sets of interchangeable collimating plates with different coatings.

3) The efficiency has a weak dependence on focal length: the longer the better.

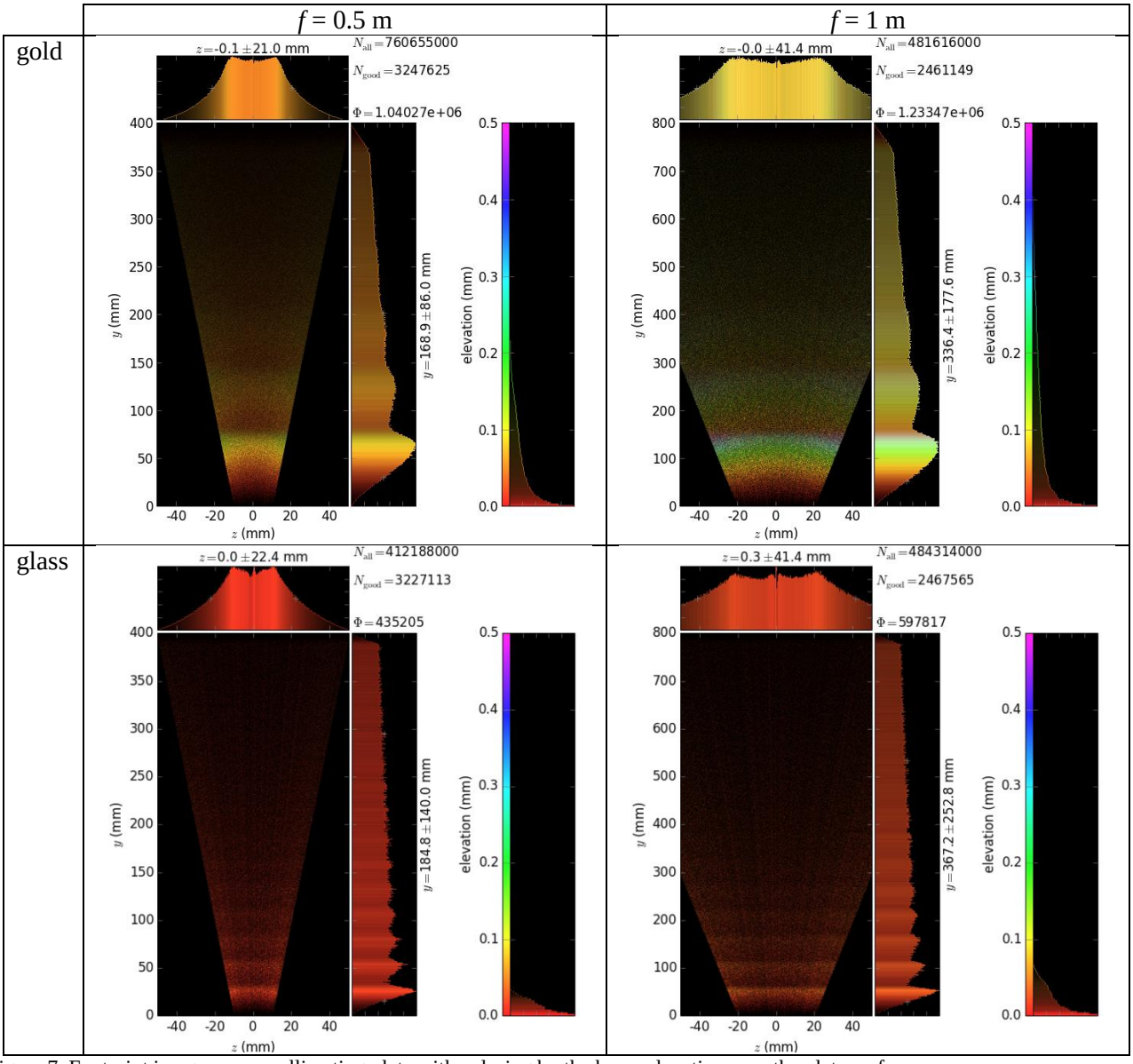

Figure 7. Footprint image over a collimating plate with coloring by the beam elevation over the plate surface.

4.2 Collective performance of multiple plates

When considering a collection of plates, another property becomes important – their thickness. When the plates come too close to the source, the spacing between them becomes comparable with the thickness. Here the thickness was selected to be 150 μm.

The properties of the collimated beam are better viewed in the collimating (sagittal) phase space, here denoted as *xx'*, see Figure 8. A glass collimator does better collimation (narrower *x'* distribution) but is less efficient. On the other hand, to use the advantage of a heavy material, one has to consider a sagittally large crystal, see the distributions width of *x*.

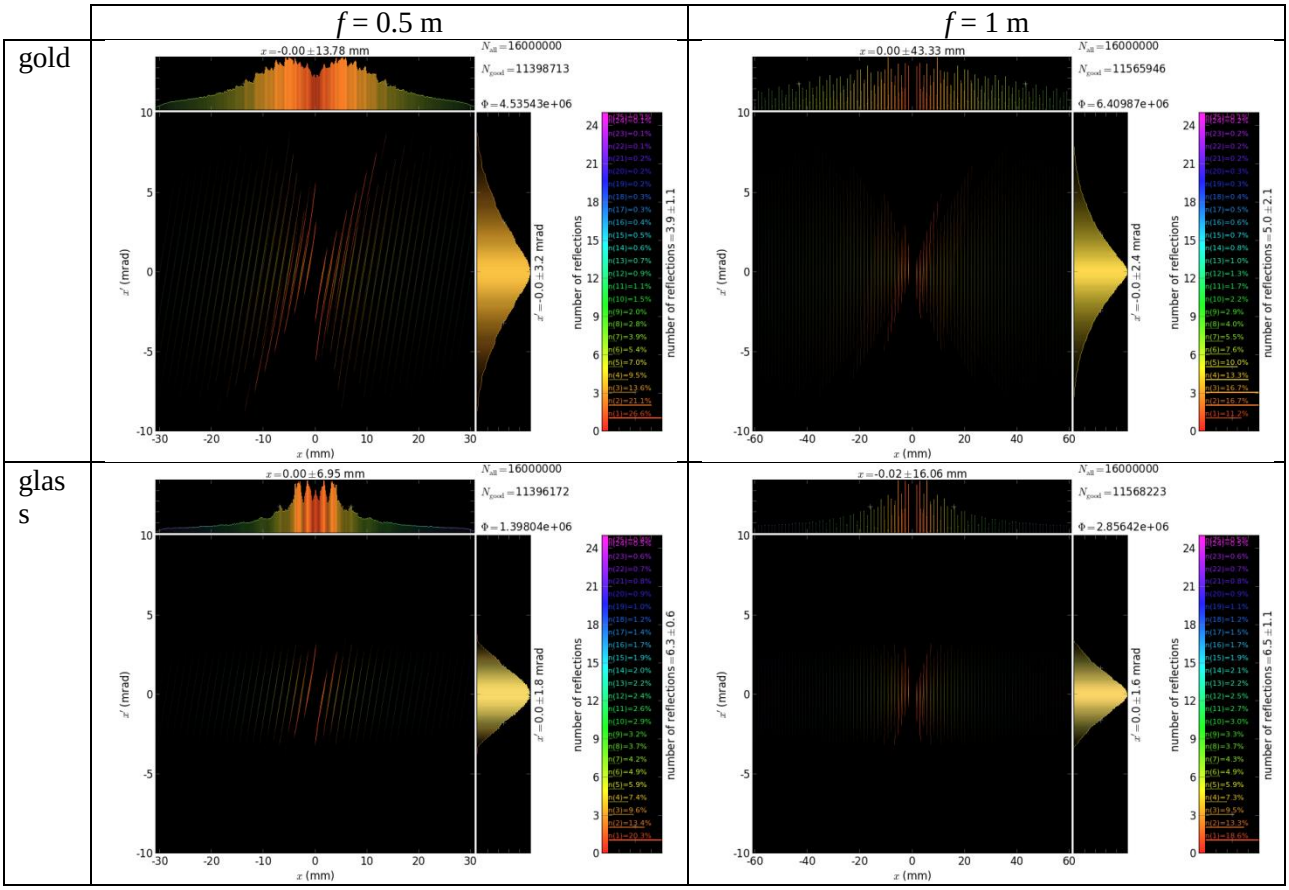

Figure 8. Sagittal phase space with coloring by the number of reflections.

4.3 Focal length

This dependence is presented in Figure 9, left. Here, the length of the plates was 0.8*f*. Even at the focal distance as short as 300 mm the losses are less than 50%. Finally, the plates should be reasonably long, with the decision based upon price and practical space constraints.

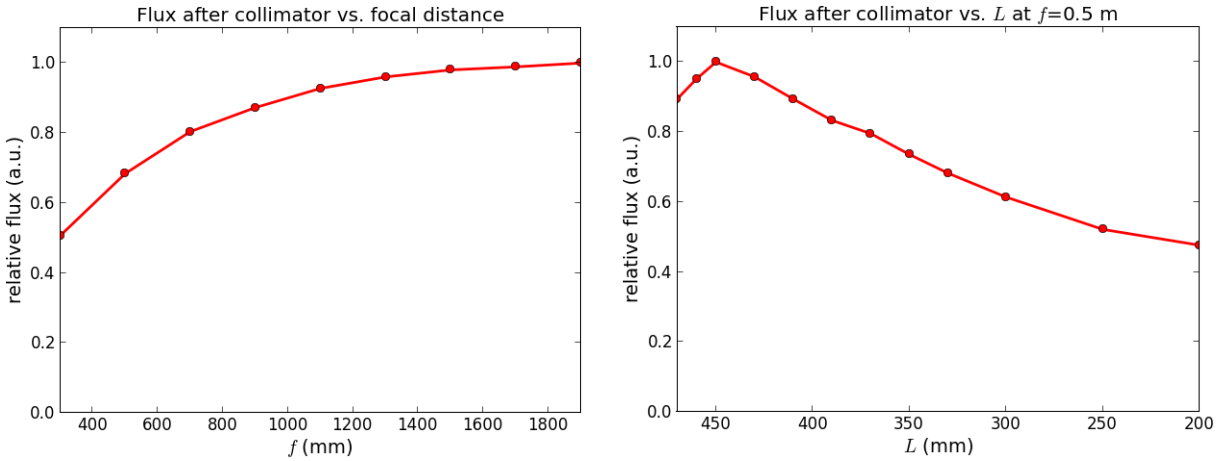

Figure 9. Left: dependence of flux downstream of the collimator on focal length. The length of the plates was also variable and equal to 0.8*f*. Right: dependence on the length of the plates *L* at a fixed focal length.

4.4 Length of plates

At a fixed focal distance the plate length L has an optimum value ~0.9f, see Figure 9, right. This behavior almost does not depend on f. This presence of the optimum is explained as follows: at too long plates, the close-to-source ends come close together and absorb a big fraction of the beam. At too short plates the reflection angles become bigger and thus the reflectivity is lowered.

4.5 Roughness

The roughness was assumed to have a normal distribution with a correlation length of 50 µm. The resulted flux starts decreasing at roughness values ~10 Å, and even at ~20 Å the losses are negligible, see Figure 10.

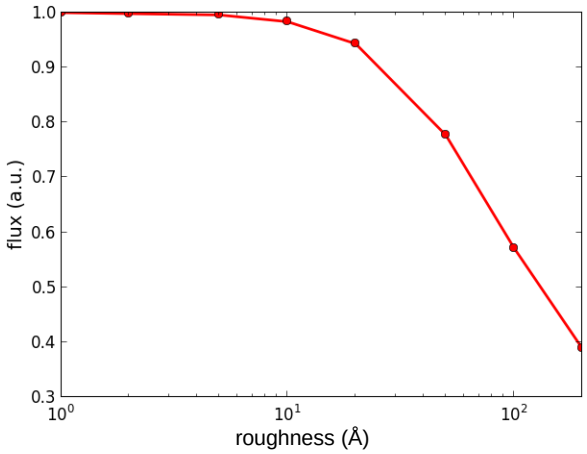

Figure 10. Dependence of flux downstream of the collimator on plate roughness.

4.6 Sagittal acceptance

The acceptance is limited by the performance of the outermost plates which deflect the incoming beam stronger than the central plates do and hence with less reflectivity. As a result, a doubled input angle does not result in a doubled flux. This effect is estimated quantitatively in Figure 11 that can be concluded as follows: 4 collimator branches which accept 50 mrad each is 2 times more efficient than one branch that accepts 200 mrad. With a low-Z material (glass) the effect is even more dramatic. The splitting of the collimator into four brunches, with correspondingly four crystals, is depicted in Figure 12. Notice that although the collimator appears to be difficult to commission, one does not need x-rays for this; a visible light source may help in the adjustment of the collimating plates.

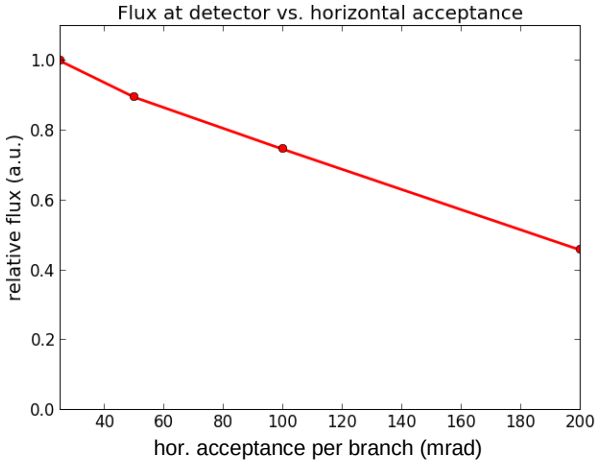

Figure 11. Dependence of flux downstream of the collimator on horizontal acceptance per branch. Notice: the total acceptance is always 200 mrad which is split here as 8×25 mrad (leftmost), 4×50 mrad, 2×100 mrad and 1×200 mrad (rightmost).

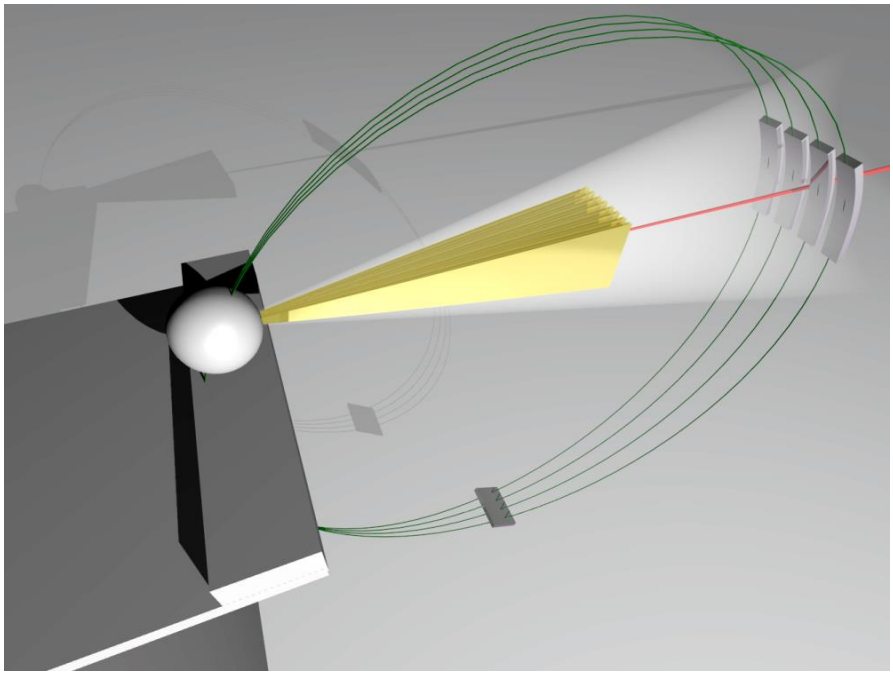

Figure 12. A 3D view of the spectrometer with a sagittal collimator. The spectrometer is split here into 4 branches.

5 Working with sagittal divergence B: sagittal segmentation of analyzing crystal

The original horizontal fan of 200 mrad is now subdivided into 4 segments, without collimation. The reason for the segmentation is twofold: to make the sagittal image size on the detector smaller and to enable several energy bands for simultaneous acquisition of several fluorescence lines. The performance of the spectrometer with and without a whispering gallery collimator (also segmented into 4 branches) is compared in this section.

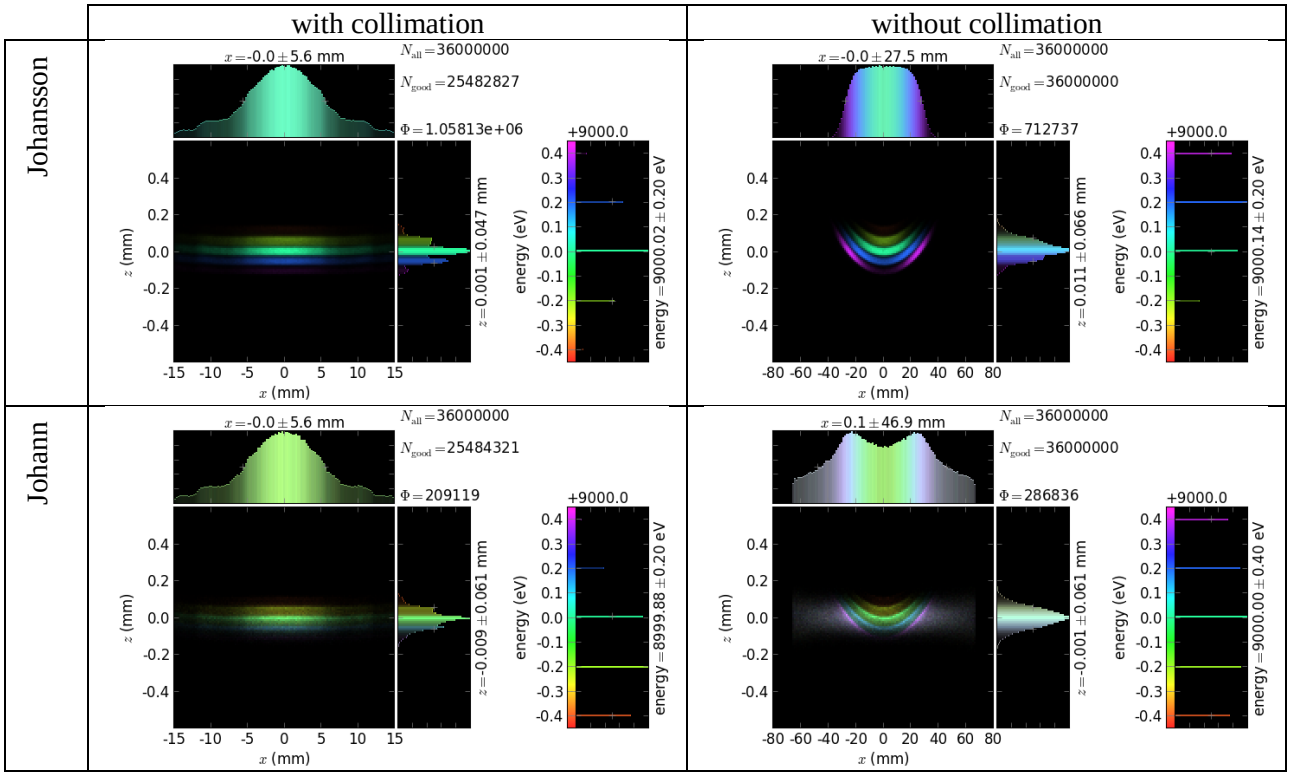

Figure 13. Detector images with and without collimation for Johansson and Johann crystals. Notice the different horizontal scales in the collimated and non-collimated cases.

The main effect of the sagittal collimation is seen on the detector images, Figure 13. Collimation makes the energy lines be horizontal, so that much simpler readout is possible, with the energy axis being simply the vertical dimension of the detector. Without collimation, the curved 2D images have to be pre-processed, using carefully taken calibration images of the elastic line. Another effect of the collimation is a much smaller sagittal size of the image.

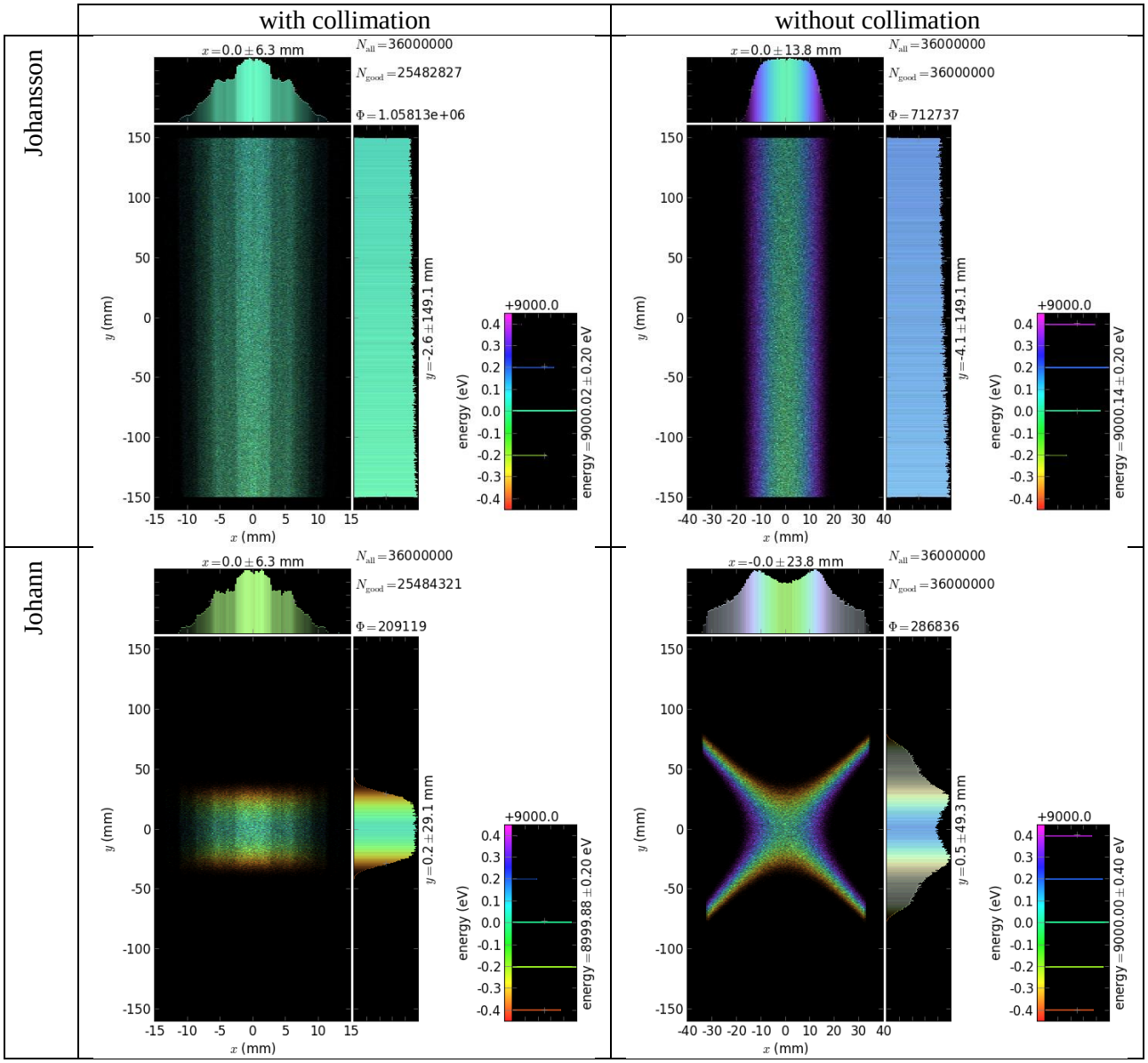

Figure 14. Crystal footprint images with and without collimation for Johansson and Johann crystals. Notice the different horizontal scales in the collimated and non-collimated cases.

In the Johansson case (ground-bent crystal) the efficiency is higher with the collimation, cf. flux values in Figure 13; in the Johann case (simply bent crystal) the result is the opposite. This fact can be understood by looking at the crystal footprints in Figure 14. A Johansson crystal provides exact point-point imaging [4], with the whole crystal in the meridional direction working for a given energy. If the beam is sagittally collimated and the beam path does not significantly differ between the central and the peripheral rays, also in the sagittal direction the crystal works for the same energy. Without collimation, a sagittally divergent beam has some sagittal energy dispersion and therefore the final efficiency depends on the source bandwidth. A Johann crystal is not exact in the meridional plane and only a central part of it works for a given energy, where the rays fall within the rocking curve. In the sagittal direction, the beam remains within this central region if it is collimated or forms hyperbola branches if it is divergent. The hyperbola braches may provide more flux than the collimated central rays, as in the present example. However, since the focusing conditions are not exact there, the branches deteriorate the energy resolution.

Notice a reduced number of "good rays" in the collimated case. These are the ones passing between the collimating plates; the rest is absorbed by the front edges.

6 Energy dispersive operation

The spectrometer can be operated in a non-scanning energy dispersive regime. This is a very attractive alternative to the usual θ-2θ energy scan, as it (i) alleviates stringent requirements on mechanical accuracy and stability and (ii) dramatically reduces the acquisition time. The energy dispersion can be attained by moving the source *into* the Rowland circle. Since the beamline focal point cannot be moved freely, it is rather the whole spectrometer that moves towards the static sample. The larger is the in-Rowland-circle shift, the wider is the accepted energy band.

The Figures 15 and 16 present the studies of the spectrometer efficiency at different in-Rowland-circle shifts, for Johansson and Johann cases and with and without sagittal collimating. The photon source was assumed to be uniform over the displayed energy band. The resulted energy distribution (the colored histogram) demonstrates the degree of flatness of the spectrometer response. As seen, a Johansson crystal provides a uniform energy response, whereas a Johann crystal is strongly non-uniform in the energy response and the intensity of the emission lines falling into its energy window will strongly depend on energy. The collimation (here with f=0.5 m) makes the energy bands on the detector to be horizontal but with less flux. Without collimation, the energy bands are curved, which results in a broader energy response even for the on-Rowland-circle case. This broadening can be mitigated by a proper pre-processing of the 2D detector images.

For the on-circle operation without collimation, the flux at the detector is $\frac{\text{detector flux}}{N\text{rays}}\frac{\text{solid angle}}{4\pi}\Phi = \frac{96\cdot10^3}{36\cdot10^6}\frac{0.2\cdot0.2}{4\pi}\cdot 10^{13} = 8\cdot10^7$ ph/s times the fluorescence quantum yield. For the in-circle position, the flux is lower proportionally to the ratio of the natural width of a line over the accepted energy band.

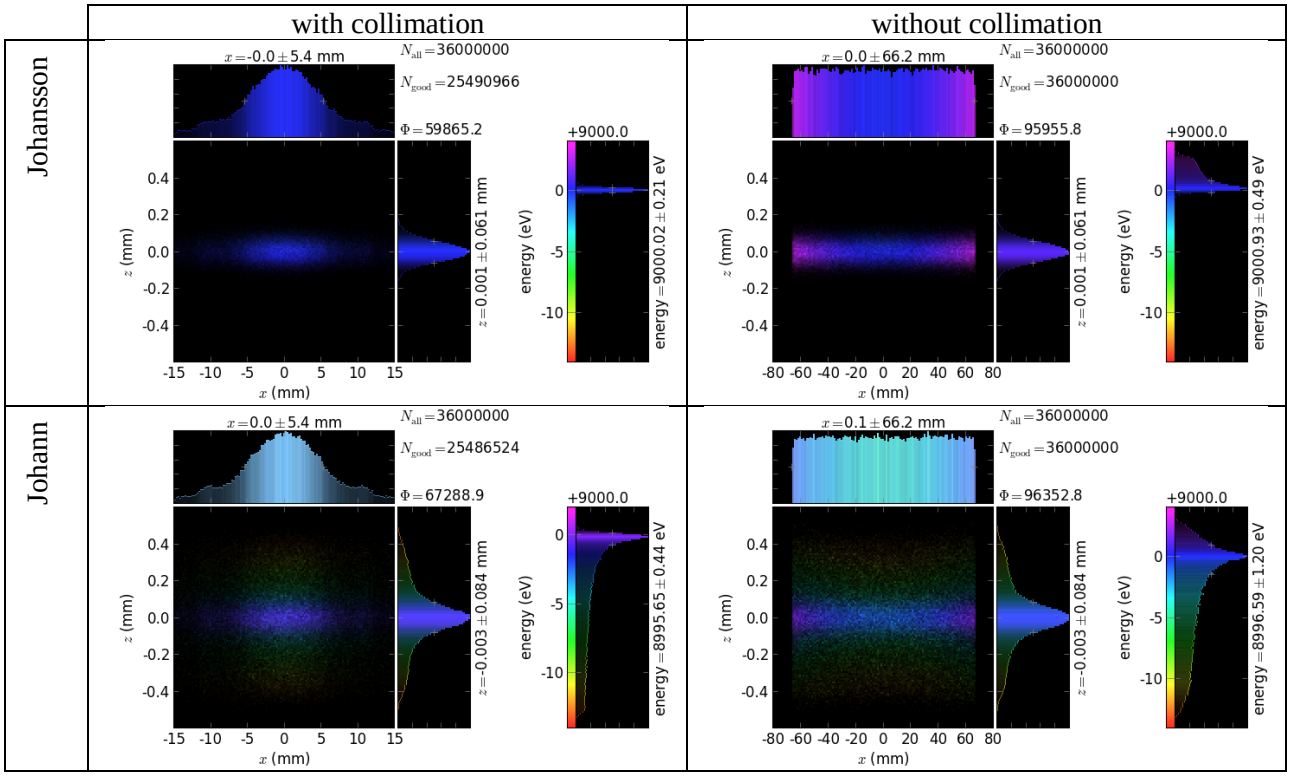

Figure 15. On-Rowland-circle sample position. Detector images of a source with uniform energy, with and without collimation for Johansson and Johann crystals. Notice the different horizontal scales in the collimated and non-collimated cases.

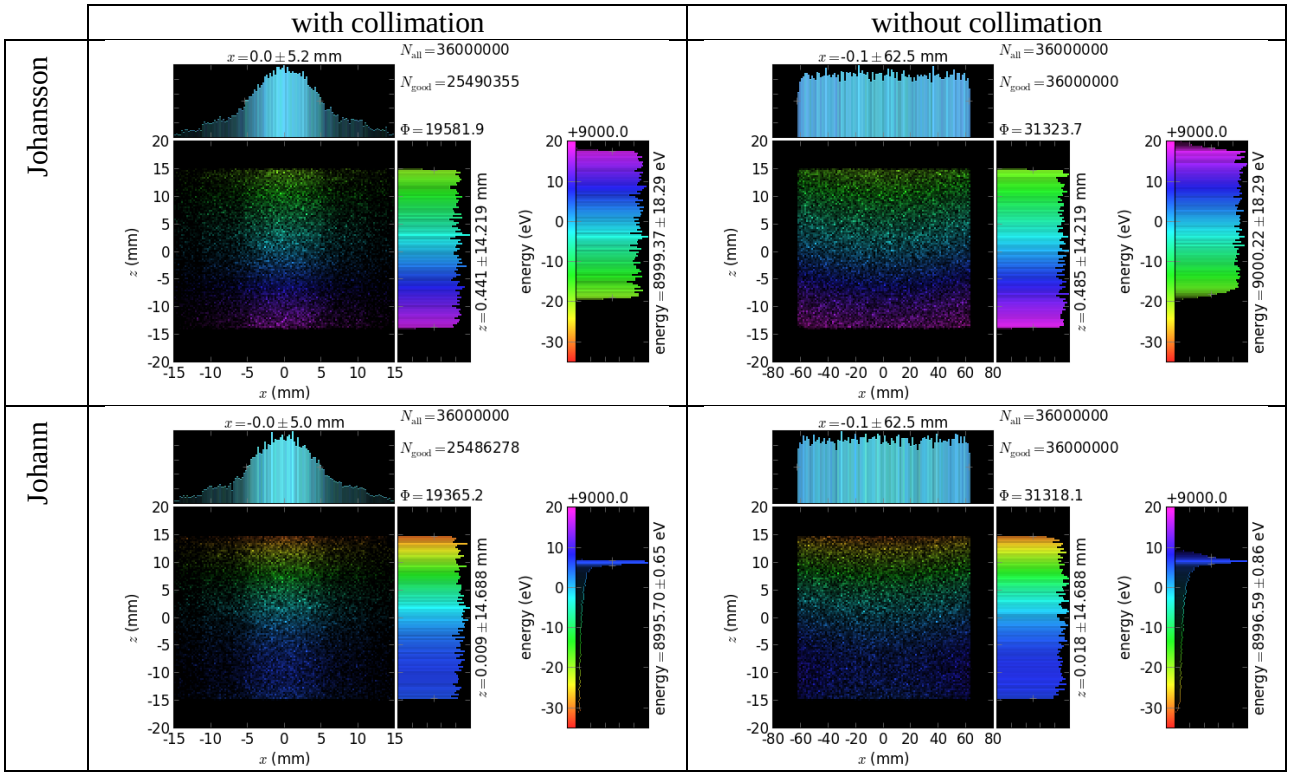

Figure 16. 50 mm in-Rowland-circle sample position. Detector images of a source with uniform energy, with and without collimation for Johansson and Johann crystals. Notice the different horizontal scales in the collimated and non-collimated cases.

7 Summary of the studies and the design proposal

To properly deal with sagittal divergence, three ways are possible:

1) to sagittally curve the crystal, as in Alba/CLEAR spectrometer,
2) to sagittally collimate the beam, e.g. with a whispering gallery collimator considered above,
3) to use a sagittally flat, possibly segmented, crystal and a 2D detector with a software analysis of the curved lines.

In these cases the complexity is, correspondingly, (1) at the crystal, (2) at the collimator and (3) at the detector. The last option seems to be (a) the simplest in manufacturing and commissioning, (b) as compared to '2', easier to use because there is nothing coming close to the sample (not any collimator) and (c) as compared to '1', more efficient because it does not have to be diced and therefore the complete surface can work for a given energy. The ground-bent (Johansson) crystals are a real must for scanning-free energy dispersive acquisition, as these provide a flat energy response.

Finally, the spectrometer is proposed to have the following characteristics:

- backward emission,
- Rowland circle diameter 1.5 m,
- 3 sets (cuts) of 4 equal Johansson crystals, sagittally flat, of size 300×~75 mm² (depends on the available detector),
- a 2D detector (a study of the today's market is required) with pixel size not larger than 50 μm; probably, there should be 2 detectors for simultaneous detection of essentially different energies, e.g. for Kα and Kβ lines,
- the detector is *under* the source-to-crystal line,
- the expected count rate for a concentrated sample is $5 \cdot 10^7$ cps at 10^{13} ph/s incoming flux.

Appendix A. Influence of Compton and Rayleigh scattering

The traditional positioning of a fluorescence detector or a fluorescence analyzer at 90^0 to the photon beam in the polarization plane has the advantage that the coherent scattering is minimized. In this case its cross section goes to zero for horizontally polarized photons. However, the elastic line *is required* for energy calibration of the curved bands in 2D detector images. In practice, for the calibration of the analyzer, the primary energy will be set close to that of the emission line(s) of interest and scanned within a few eV while measuring the 2D detector images of the elastically scattered light.

For light elements, Compton scattering can be more intense than Rayleigh scattering in the energy range of interest (2–30 keV). The Compton peak is rather wide because of multiple Compton scattering and scattering off valence electrons. The Compton wavelength shift $\Delta\lambda=\lambda_C(1-\cos\theta)$ is zero for the forward scattering and maximal for the back scattering. It appears that the scattered photons which initially had energy near a K-absorption edge have the final energy near and below the corresponding Kβ line energy for scattering at 90^0. Back scattering (180^0) leads to a larger shift, away from the Kβ line, thus enabling cleaner Kβ spectroscopy, see Figure 17.

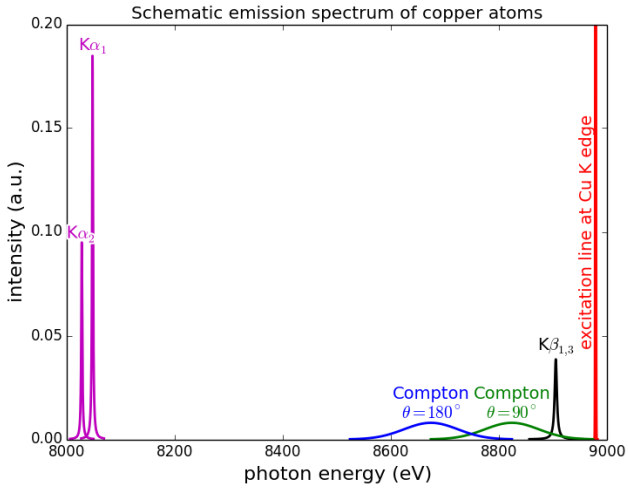

Figure 17. Schematic emission spectrum of copper atoms at the excitation at the Cu K-edge. The relative intensities and widths of Kα and Kβ lines are taken as tabulated [5]. The intensity and width of Compton peaks are arbitrary; the position was calculated from the wavelength shift.

A.1. Experimental study of Compton and elastic scattering

We performed a simple angle dependent study of the scattering off a light sample (Kapton) by using a single pixel silicon drift detector [6]. Due to the space restrictions, the detector could not be positioned very close to 0^0 and 180^0. The most forward direction was at 68^0, and the most backward angle was 139^0. These two positions were compared with the usual orthogonal direction, see Figure 18. The scattering was in-plane with the nominal polarization vector (horizontal), at the energy of the incident beam 9 keV. The sampling time was 100 s for each position. The output count rate is dead-time corrected.

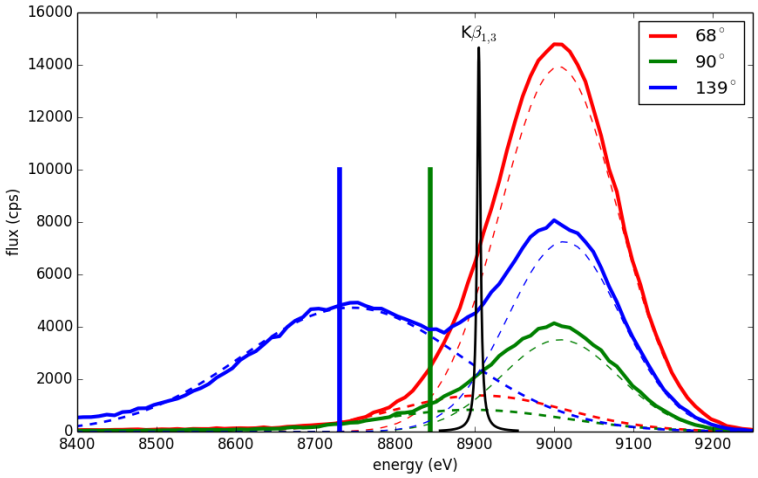

Figure 18. Measured output from the multi-channel analyzer. The dashed lines are results of fitting. The vertical lines are energy positions as calculated by the Compton shift. The imaginary Kβ line (copper was not present in the sample) has an arbitrary amplitude.

First of all, one can see that at 90^0 scattering the intensity of the elastic line is not that low. The reason is probably multiple scattering and the presence of unpolarized photons. The contribution of Compton scattering can be isolated by peak-fitting assuming Gaussian line shapes. It appears that the width of the elastic line is almost the same for all the angles, and thus it is purely due to the detector resolution, whereas the width of the Compton line slightly increases with the scattering angle. We then subtracted the squared sigma of the elastic line from that of the Compton line in order to demonstrate the expected Compton line (rather a band) as should be seen by a high resolution analyzer, see Figure 19.

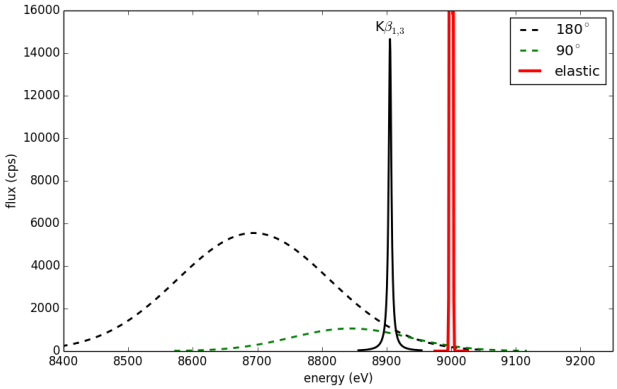

Figure 19. Expected Compton bands (dashed lines) after removal of the broadening due to finite energy resolution.

As seen, the contribution of Compton scattering in the vicinity of the Kβ line is similar for the cases of 90^0 and 180^0 scattering angles. The idealized Gaussian shape is in reality skewed such that the low energy tail is longer due to multiple Compton scattering, and the high energy tail is shorter. Therefore the Figure 19 gives a somewhat pessimistic picture for the 180^0 case.

Appendix B. Comparison with von Hamos spectrometer

A von Hamos spectrometer has axial symmetry around the axis connecting the source and the detector [7]. The analyzing crystal is cylindrically bent with the radius equal to the crystal-to-axis distance. In this scheme, the emission escape direction depends on the Bragg angle (energy), see Figure 20 (a). In practice, the spectrometer axis is adapted such that the escape direction is appropriate for a given sample setup. In particular, the escape direction can be kept in back scattering (relatively to the sample), see Figure 20 (b). In the latter case the mechanical model is more complex and includes three translations and two rotations.

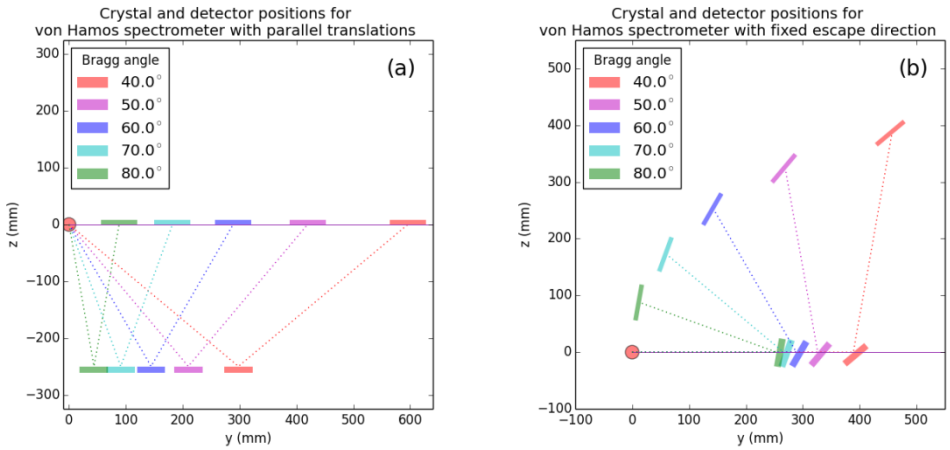

Figure 20. Crystal (shorter bars) and detector (longer bars) positions in von Hamos geometry. The crystal is sagittally curved around the source–detector line. The detector plane is perpendicular to the sketch. (a) The classical setup with 2 translations. (b) The setup with an invariant escape direction.

In order to compare energy resolution and efficiency, the geometrical parameters for a von Hamos spectrometer were taken from [8]: a diced 100 (sagittal) × 50 (meridional) mm² Si(444) crystal is curved with R_s = 250 mm. The width of segmented facets was taken equal to 5 mm (as in [8]) and 1 mm together with a continuously bent case. The Johann and Johansson crystals were taken for a 1-m-diameter Rowland circle (as mostly common worldwide), in the square shape with 100 mm sides. An additional case was also included: the Johann crystal was rotated by 90^0 around the sample-to-crystal line and thus became a von

Hamos crystal that had to be put at a correct distance corresponding to the 1 m sagittal radius. The source size was 100×100 μm².

In comparing with a Hamos spectrometer, one should realize its strongest advantage – inherent energy dispersive operation without a need for energy scan. This advantage is especially important for broad emission lines. Below, the comparison is made for two cases: (1) a narrow energy band (Figure 21, left), which is more interesting for valence band RIXS and which assumes a high resolution monochromator in the primary beam and (2) a wide energy band (Figure 21, right), which is more interesting for core state RIXS and normal fluorescence detection. The desired position on the charts is in the upper left corner. As seen in Figure 21, the efficiency of the von Hamos crystals (i) is independent of the energy band (equal for the left and right charts), which demonstrates truly energy-dispersive behavior of the crystals but (ii) is significantly lower as compared to the Johann and Johansson crystals. The reason for the lower efficiency can be understood from Figure 22, where the magnified footprint on the crystal is shown: only a narrow line on the crystal contributes to a given energy band. Here, for a bandwidth of 2.4 eV only ~0.5 mm of the crystal is in use. A way to increase efficiency is to place the crystal closer to the source, which obviously worsens energy resolution because of the increased angular source size. Inversely, if the crystal is put at a further distance, the energy resolution is improved (square symbols in Figure 21) but the efficiency is low because of a smaller solid angle collected.

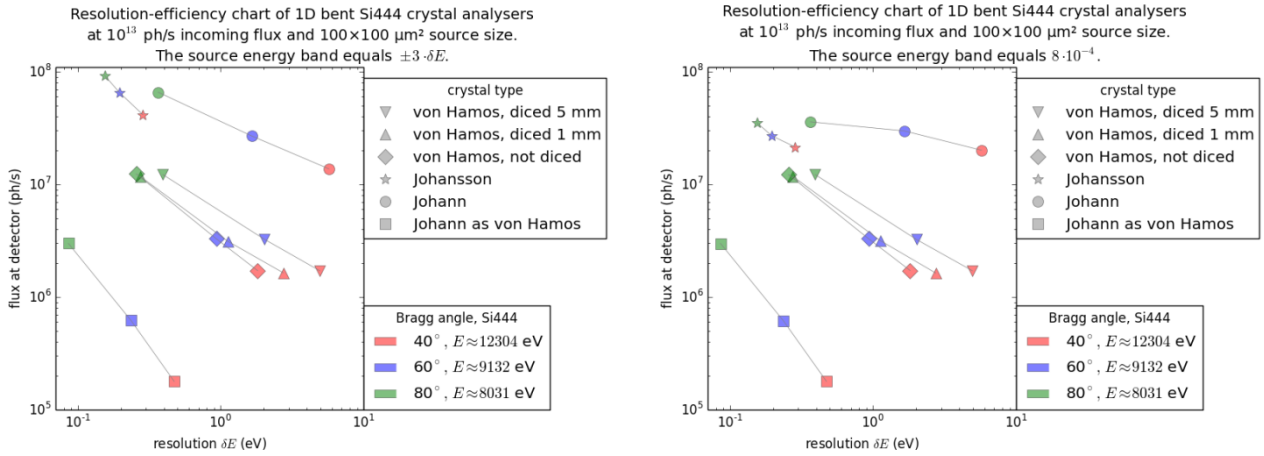

Figure 21. Resolution-efficiency charts for 1D bend crystal analyzers. Left: with a narrow energy band equal to the 6-fold energy resolution. Right: with a wide energy band equal to $8 \cdot 10^{-4} E$ (approximate width of K β lines [5]).

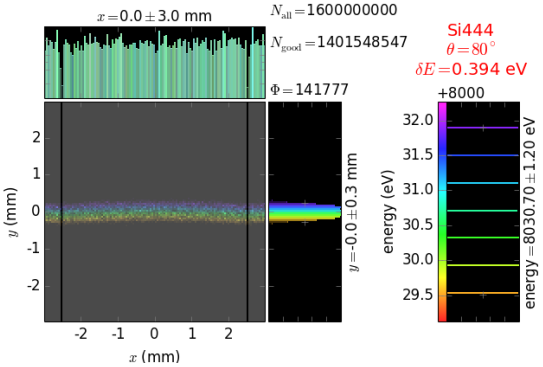

Figure 22. Zoomed-in footprint on the 5-mm-diced von Hamos crystal.

Finally, among the compared 1D-bent spectrometers the Johansson type is the best in the combination of good energy resolution and high efficiency. It is the only one that can function both as a high resolution spectrometer *and* a fluorescence detector. One should bear in mind, however, two very strong advantages of von Hamos spectrometers: (1) they do not need alignment – a crystal and a detector positioned approximately will most probably immediately work and (2) the image is inherently energy dispersive with a flat (energy independent) detector response. The low efficiency and mediocre energy resolution are a price for the commissioning-free energy dispersive operation. Rowland circle based spectrometers will always require good alignment, and among them only the Johansson-type spectrometer can be made energy dispersive with a flat detector response, see Section 6.

References

[1] https://www.cells.es/en/beamlines/bl22-claess/doc-conceptualdesignxrayspectrometer_claess

[2] K. Klementiev and R. Chernikov, "Powerful scriptable ray tracing package xrt," in Advances in Computational Methods for X-Ray Optics III, M. Sanchez del Rio and O. Chubar, eds. (Proc. SPIE 9209, 2014), p. 92090A.
pypi.python.org/pypi/xrt,
pythonhosted.org/xrt

[3] en.wikipedia.org/wiki/Whispering-gallery_wave,
en.wikipedia.org/wiki/Whispering_gallery

[4] T. Johansson, Z. Phys. **82** (1933) 507.

[5] X-Ray Data Booklet, xdb.lbl.gov/
M. O. Krause and J. H. Oliver, J. Phys. Chem. Ref. Data **8** (1979) 329.

[6] K. Sigfridsson, K. Norén, K. Klementiev (2014), unpublished, data from beamline I811 at MAX II storage ring.

[7] L. von Hamos, Naturwiss. **20** (1932) 705.

[8] J. Szlachetko, M. Nachtegaal, E. de Boni, M. Willimann, O. Safonova, J. Sa, G. Smolentsev, M. Szlachetko, J. A. van Bokhoven, J.-Cl. Dousse, J. Hoszowska, Y. Kayser, P. Jagodzinski, A. Bergamaschi, B. Schmitt, C. David, and A. Lücke, Rev. Sci. Instrum. **83** (2012) 103105.